Evaluation of thermal helium beam and line-ratio fast diagnostic on the National Spherical Torus Experiment-Upgrade

J. M. Muñoz Burgos, M. Agostini, P. Scarin, D. P. Stotler, E. A. Unterberg, S. D. Loch, O. Schmitz, K. Tritz, and D. Stutman

Articles you may be interested in

Fast Thermal Helium Beam diagnostic for measurements of edge electron profiles and fluctuations
Rev. Sci. Instrum. **86**, 123513 (2015); 10.1063/1.4939003

Supersonic helium beam diagnostic for fluctuation measurements of electron temperature and density at the Tokamak TEXTOR
Rev. Sci. Instrum. **83**, 065107 (2012); 10.1063/1.4707150

Hybrid time dependent/independent solution for the He I line ratio temperature and density diagnostic for a thermal helium beam with applications in the scrape-off layer-edge regions in tokamaks
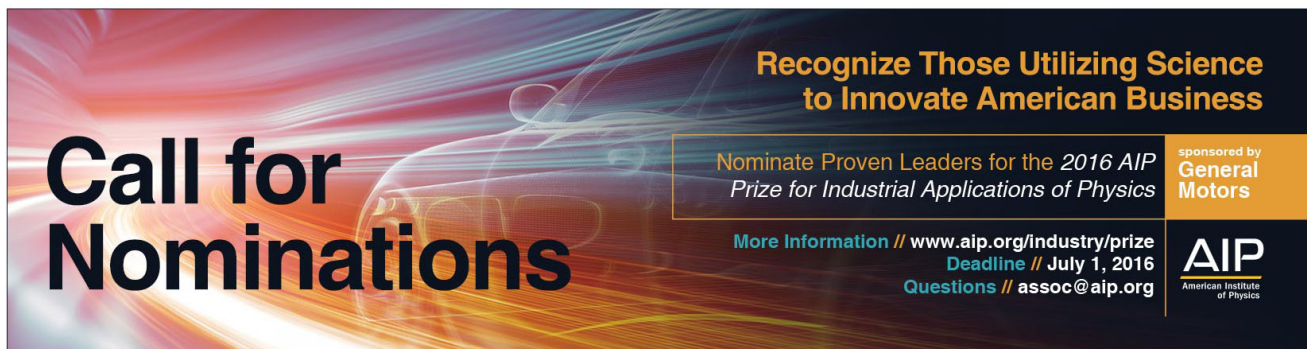Phys. Plasmas **19**, 012501 (2012); 10.1063/1.3672230

Emission intensities and line ratios from a fast neutral helium beam
Phys. Plasmas **14**, 083301 (2007); 10.1063/1.2759191

Survey of diagnostic systems for the study of gyrocenter shifts on National Spherical Torus Experiment
Rev. Sci. Instrum. **77**, 10F505 (2006); 10.1063/1.2220079

Evaluation of thermal helium beam and line-ratio fast diagnostic on the National Spherical Torus Experiment-Upgrade

J. M. Muñoz Burgos,[1,a)] M. Agostini,[2,b)] P. Scarin,[2,c)] D. P. Stotler,[3,d)] E. A. Unterberg,[4,e)] S. D. Loch,[5,f)] O. Schmitz,[6,g)] K. Tritz,[1,h)] and D. Stutman[1,i)]

[1]*Department of Physics and Astronomy, Johns Hopkins University, Baltimore, Maryland 21218, USA*
[2]*Consorzio RFX (CNR, ENEA, INFN, Universita di Padova, Acciaierie Venete SpA), Corso Stati Uniti 4, 35127 Padova, Italy*
[3]*Princeton Plasma Physics Laboratory, Princeton, New Jersey 08543, USA*
[4]*Oak Ridge National Laboratory, Oak Ridge, Tennessee 37831, USA*
[5]*Department of Physics, Auburn University, Auburn, Alabama 36849, USA*
[6]*Department of Engineering Physics, University of Wisconsin-Madison, Madison, Wisconsin 53706, USA*

A 1-D kinetic collisional radiative model with state-of-the-art atomic data is developed and employed to simulate line emission to evaluate the Thermal Helium Beam (THB) diagnostic on NSTX-U. This diagnostic is currently in operation on RFX-mod, and it is proposed to be installed on NSTX-U. The THB system uses the intensity ratios of neutral helium lines 667.8, 706.5, and 728.1 nm to derive electron temperature (eV) and density (cm^{-3}) profiles. The purpose of the present analysis is to evaluate the applications of this diagnostic for determining fast ($\backsim 4\,\mu s$) electron temperature and density radial profiles on the scrape-off layer and edge regions of NSTX-U that are needed in turbulence studies. The diagnostic is limited by the level of detection of the 728.1 nm line, which is the weakest of the three. This study will also aid in future design of a similar 2-D diagnostic system on the divertor. *Published by AIP Publishing.*
[http://dx.doi.org/10.1063/1.4948554]

I. INTRODUCTION

Helium line-ratio diagnostic for determining electron temperatures and densities is a standard and important technique applied on measurements of plasma edge, scrape-off layer (SOL), and divertor regions on several fusion experiments such as TEXTOR,[1,2] RFX-mod,[3] PISCES-B,[4] JET,[5] and JT-60U.[6] Helium emission has been used for edge turbulence measurements using the Gas-Puff Imaging (GPI) system on NSTX,[7] for validation of plasma transport models on MAST[8] and for edge turbulence characterization on RFX-mod.[9,10]

Until recently, this powerful diagnostic technique was limited by the quality of atomic data available. Precise calculations of the near threshold resonances in the cross-sections are needed for accurate spectral line-ratio diagnostics,[11] particularly for temperatures below the ionization potential. This diagnostic technique has also been limited by neglecting the time-evolution of the triplet spin system of the metastable state of helium.[8,12] Figure 1 shows the two spin systems of helium.

A new Hybrid-Time-Dependent/Independent (HTD/I) helium line-ratio model that employs state-of-the-art R-Matrix,[13]

R-Matrix With Pseudostates (RMPS),[14] Convergent Close Coupling (CCC) electron-impact excitation and ionization data[15,16] and that takes into account the transient relaxation times of the atomic states has been developed.[12] This new HTD/I model extends the spatial range of electron temperature and density measurements, and improves agreement with Multi-Point Thomson Scattering (MPTS)
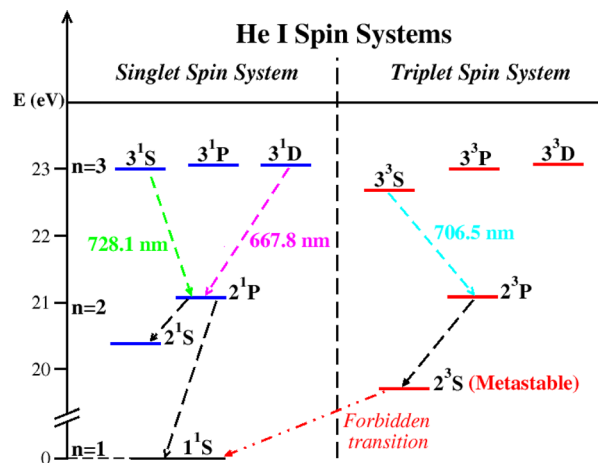

FIG. 1. Helium contains two spin systems: The singlet (^1S ground state) and the triplet (^3S metastable state). The electron temperature sensitive line-ratio (706.5/728.1) becomes time dependent due to the long relaxation time of the metastable state (^3S) at low electron densities ($n_e \leq 10^{12}$ cm^{-3}),[12] and which populates the 706.5 nm line in comparison to the 728.1 nm line that is populated from the singlet ground state (^1S). The electron density sensitive line-ratio (667.8/728.1) is time independent (short relaxation times), because both of these lines are dominantly populated from the singlet ground state (^1S).[12]

a)Electronic mail: jmunozbu@pppl.gov.
b)Electronic mail: matteo.agostini@igi.cnr.it.
c)Electronic mail: paolo.scarin@igi.cnr.it.
d)Electronic mail: dstotler@pppl.gov.
e)Electronic mail: unterberge@fusion.gat.com.
f)Electronic mail: loch@physics.auburn.edu.
g)Electronic mail: oschmitz@wisc.edu.
h)Electronic mail: ktritz@pppl.gov.
i)Electronic mail: dstutma1@jhu.edu.

measurements[2,12] when compared to the widely used helium atomic model developed at TEXTOR.[1]

In this work, a 1-D kinetic collisional radiative solution is developed and used to simulate helium emission from a helium gas-puff. This model employs the same state-of-the-art atomic data as the HTD/I helium line-ratio model, and has also the capability to include the effects of high Rydberg state contributions to the lower atomic populations. The model also includes helium–proton charge-exchange effects using newly calculated state-of-the-art cross-sections.[17] Electron and ion ionization rate-coefficients were compared to charge-exchange in order to quantify the magnitude of each of the depletion process acting on the neutral gas-puff.

In the second part of this paper, the HTD/I helium line-ratio model is used to analyze measured emission data from RFX-mod to obtain electron temperature and density radial profiles from the thermal helium beam (THB) diagnostic.[10] These profiles were compared to those derived using the TEXTOR helium model that is typically employed to analyze the experimental data on RFX-mod.[1]

In the third part, the 1-D kinetic collisional model is used to simulate line emission of a thermal helium gas-puff as it propagates along the radial direction of NSTX for the 667.8, 706.5, and 728.1 nm lines. The simulated line intensities were used to evaluate the sensitivity of the THB system, and to assess the application of this diagnostic on NSTX-U. Additionally, electron temperature and density radial profiles were derived using the HTD/I line-ratio model[12] and compared to the initial profiles. Perturbative effects on the plasma and opacity of different emission lines are also discussed.

II. KINETIC COLLISIONAL RADIATIVE MODEL

To successfully model spectral emission from a thermal gas injector in the Scrape-Off Layer (SOL) and edge regions of NSTX, it is necessary to include the main atomic collision interactions that contribute to both emission and depletion of the neutral gas in a kinetic collisional radiative model (CRM). Any ion/atom can be modeled by a set of terms (LS-coupling) with interacting radiative and collisional couplings. In the SOL/edge plasma regions, the processes that play the main role in populating/de-populating (e.g., $A_{nl \to ml'}$ de-populates the nl-state) the various nl-terms may include:

- Radiative decay: $[A_{ml' \to nl}/A_{nl \to ml'}]$
- Electron-impact excitation/de-excitation: $[q^e_{ml' \to nl}/q^e_{nl \to ml'}]$
- Electron-impact ionization: $[S^e_{nl}]$
- Charge-exchange: $[\sigma^{CX}_{nl}]$

Electron recombination is not included in the model, and it is assumed that any neutral atom in the gas-puff that is ionized gets trapped in the magnetic field lines and transported away from the view of the detector. This transported ion may eventually recycle/recombine and continue emitting at the same wavelengths as the neutrals from the gas-puff injection; therefore, by subtracting the background and gas-puff signals, the recombination contributions are removed (See Figure 4).

Any given neutral atom interacting with a plasma in the excited nl-term can be represented using the kinetic equation

with the atomic collisional processes (on the right hand side) included

$$\frac{\partial f_{nl}}{\partial t} + \boldsymbol{v} \cdot \nabla f_{nl} = \sum_{nl \neq ml'} \left[A_{ml' \to nl} + n_e q^e_{ml' \to nl} \right] f_{ml'}$$
$$- \left\{ n_i q^{CX}_{nl}(\boldsymbol{v}) + n_e S^e_{nl} \right.$$
$$\left. + \sum_{nl \neq ml'} \left[A_{nl \to ml'} + n_e q^e_{nl \to ml'} \right] \right\} f_{nl}, \quad (1)$$

where n_e and n_i are the free electron/ion densities, and $f_{nl}(\boldsymbol{v}, \boldsymbol{r}, t)$ represents the neutral atom distribution function in the excited nl-term. The velocity-dependent charge-exchange rate-coefficient is defined by the collision integral

$$q^{CX}_{nl}(\boldsymbol{v}) = \frac{1}{n_i} \int d^3 \boldsymbol{v}' |\boldsymbol{v} - \boldsymbol{v}'| \sigma^{CX}_{nl}(|\boldsymbol{v} - \boldsymbol{v}'|) f_i(\boldsymbol{v}'), \quad (2)$$

with a free ion distribution function represented in the form of a shifted Maxwellian by an ion flow velocity $\boldsymbol{v}_i$ in the form

$$f_i(\boldsymbol{v}) = \frac{n_i}{\pi^{3/2} v^3_{th_i}} e^{-(v - v_i)^2 / v^2_{th_i}}, \quad (3)$$

and a thermal ion velocity defined as

$$v_{th_i} = \sqrt{\frac{2 k_B T_i}{m_i}}. \quad (4)$$

In order to solve the kinetic Equation (1), the distribution function of the injected neutrals is assumed to be in the form

$$f_{nl}(\boldsymbol{v}, \boldsymbol{r}, t) = f_o(\boldsymbol{v}) n_{nl}(\boldsymbol{r}, t), \quad (5)$$

where $n_{nl}(\boldsymbol{r}, t)$ represents the density population of the nlth excited term as a function of position and time, and the velocity dependent function $f_o(\boldsymbol{v})$ has the form of a shifted Maxwellian distribution with a given displacement velocity $\boldsymbol{v_n}$

$$f_o(\boldsymbol{v}) = \frac{1}{\pi^{3/2} v^3_{th_n}} e^{-(v - v_n)^2 / v^2_{th_n}}. \quad (6)$$

It has been shown that the particle velocity distribution of the puff can be described by a drifting narrowed Maxwellian distribution with flow velocity $v_n = M \sqrt{\gamma k_B T_n / m_n}$,[18] where M is the Mach number ($M = 1$ for this case), γ is the specific heat ratio ($\gamma = 5/3$ for helium), T_n is the neutral gas temperature ($T_n \approx 300$ K), and m_n is the mass of the neutrals in the gas.[18]

The gas-puff flow and thermal velocity of the neutrals are given by

$$v_n = \sqrt{\frac{5 k_B T_n}{3 m_n}}$$
$$v_{th_n} = \sqrt{\frac{2 k_B T_n}{m_n}}. \quad (7)$$

Equation (1) can be integrated with respect to velocity by substituting the distribution function solution from Equation (5) using the integral relations

$$n_{nl} = \int d^3\boldsymbol{v} f_{nl}$$

$$n_{nl}\boldsymbol{v_n} = \int d^3\boldsymbol{v}\boldsymbol{v} f_{nl}, \tag{8}$$

which yield

$$\frac{\partial n_{nl}}{\partial t} + \boldsymbol{v_n} \cdot \nabla n_{nl} = \sum_{nl \neq ml'} \left[A_{ml' \to nl} + n_e q^e_{ml' \to nl}\right] n_{ml'}$$
$$- n_i \int d^3\boldsymbol{v} q^{CX}_{nl}(\boldsymbol{v}) f_{nl}$$
$$- \left\{ n_e S^e_{nl} + \sum_{nl \neq ml'} \left[A_{nl \to ml'} + n_e q^e_{nl \to ml'}\right] \right\} n_{nl}. \tag{9}$$

From the definition of the charge-exchange rate-coefficient given in Equation (2), the charge-exchange collision integral can be written as

$$n_i \int d^3\boldsymbol{v} q^{CX}_{nl}(\boldsymbol{v}) f_{nl} = \int d^3\boldsymbol{v} f_{nl}(\boldsymbol{v}, \boldsymbol{r}, t)$$
$$\times \int d^3\boldsymbol{v'} |\boldsymbol{v} - \boldsymbol{v'}| \sigma^{CX}_{nl}(|\boldsymbol{v} - \boldsymbol{v'}|) f_i(\boldsymbol{v'}), \tag{10}$$

which can be integrated and written in the form

$$n_i \int d^3\boldsymbol{v} q^{CX}_{nl}(\boldsymbol{v}) f_{nl} = n_i Q^{CX}_{nl} n_{nl}. \tag{11}$$

The generalized charge-exchange rate-coefficient Q^{CX}_{nl} is obtained from the collision integral Equation (10) [Equation (A11)], and the derivation is shown in detail in the Appendix. The solution is given by

$$Q^{CX}_{nl} = \frac{2}{\sqrt{\pi}} \frac{\left(v^2_{th_i} + v^2_{th_n}\right)}{|\boldsymbol{v_i} - \boldsymbol{v_n}|} e^{-(v_i - v_n)^2 / \left(v^2_{th_i} + v^2_{th_n}\right)}$$
$$\times \int_0^\infty d\nu \nu^2 \sin h \left[\frac{2|\boldsymbol{v_i} - \boldsymbol{v_n}|}{\sqrt{v^2_{th_i} + v^2_{th_n}}} \nu\right] \sigma^{CX}_{nl}(\nu) e^{-\nu^2}, \tag{12}$$

where the non-dimensional quantity ν is defined as a function of the center of mass energy as

$$\nu = \frac{1}{\sqrt{v^2_{th_i} + v^2_{th_n}}} \sqrt{\frac{2eE(\text{eV/amu})}{m_{amu}}}. \tag{13}$$

Substituting Equation (11) into Equation (9), and by choosing the propagation velocity axis of the gas-puff along the radial direction, $\boldsymbol{v_n} = v_n\hat{r}$ yields

$$\frac{\partial n_{nl}}{\partial t} + v_n \frac{\partial n_{nl}}{\partial r} = \sum_{nl \neq ml'} \left[A_{ml' \to nl} + n_e q^e_{ml' \to nl}\right] n_{ml'}$$
$$- \left\{ n_i Q^{CX}_{nl} + n_e S^e_{nl} \right.$$
$$\left. + \sum_{nl \neq ml'} \left[A_{nl \to ml'} + n_e q^e_{nl \to ml'}\right] \right\} n_{nl}. \tag{14}$$

Equation (14) can be written in terms of the collisional radiative matrix as

$$\frac{\partial n_{nl}}{\partial t} + v_n \frac{\partial n_{nl}}{\partial r} = \sum_{nl \neq ml'} C_{nl,ml'} n_{ml'} + C_{nl,nl} n_{nl}, \tag{15}$$

where the non-diagonal elements of the matrix (gains) are represented by

$$C_{nl,ml'} = A_{ml' \to nl} + n_e q^e_{ml' \to nl}, \tag{16}$$

and the diagonal elements (losses) by

$$C_{nl,nl} = -\left\{ n_i Q^{CX}_{nl} + n_e S^e_{nl} \right.$$
$$\left. + \sum_{nl \neq ml'} \left[A_{nl \to ml'} + n_e q^e_{nl \to ml'}\right] \right\}. \tag{17}$$

The atomic data used in the CRM are the same as the one from the HTD/I helium line-ratio model,[12] and the present model also includes helium–deuteron charge-exchange interactions by employing newly calculated state-of-the art cross-sections[17] to obtain the generalized charge-exchange rate-coefficients Q^{CX}_{nl} [Equation (12)].

In the SOL region of the tokamak, the D^+ ions move with a flow velocity $\boldsymbol{v_i}$ [Equation (3)] parallel to the magnetic field lines, and with a magnitude equal to the plasma sound speed $v_i = \sqrt{k_B(T_e + T_i)/(m_e + m_i)}$.[19] In this work, the electron/ion (protons) temperatures and densities are assumed to be equal ($T_i \approx T_e$ and $n_i \approx n_e$);[19] therefore, the magnitude of the ion flow velocity is $v_i \approx \sqrt{2k_B T_e/(m_e + m_i)}$. The gas-puff injection axis is mostly perpendicular to the magnetic field lines in the SOL; therefore, it is safe to assume that $\boldsymbol{v_n} \perp \boldsymbol{v_i}$, and $|\boldsymbol{v_i} - \boldsymbol{v_n}| \approx \sqrt{v_i^2 + v_n^2}$ in Equation (12).

The sum in the collisional radiative matrix is performed for a total of $N = 19$ terms for the configurations $1snl$ ($1s < nl < 4f$).[12] In order to account for high Rydberg state contributions to the lower states, the projection matrix can be included in the calculation.[12] The comprehensive collisional radiative matrix is obtained by adding the indirect contributions of the high Rydberg states to the $N = 19$ terms of the direct contributions [Equations (16) and (17)].[12]

One of the standard techniques for solving first order partial differential equations is to integrate along characteristics. By choosing s as the variable along the characteristic, the following relation is used

$$\frac{dn_{nl}}{ds} = \frac{dt}{ds} \frac{\partial n_{nl}}{\partial t} + \frac{dr}{ds} \frac{\partial n_{nl}}{\partial r}, \tag{18}$$

where $\frac{dt}{ds} = 1$, and $\frac{dr}{ds} = v_n$. Therefore, Equation (15) can be expressed in the reduced form

$$\frac{dn_{nl}}{ds} = \sum_{nl \neq ml'} C_{nl,ml'} n_{ml'} + C_{nl,nl} n_{nl}.$$ (19)

Rewriting Equation (19) in matrix form for a N total number of nl-terms

$$\begin{pmatrix} \frac{dn_1}{ds} \\ \frac{dn_2}{ds} \\ \vdots \\ \frac{dn_N}{ds} \end{pmatrix} = \begin{pmatrix} C_{1,1} & C_{1,2} & \dots & C_{1,N} \\ C_{2,1} & C_{2,2} & \dots & C_{2,N} \\ \vdots & \vdots & \ddots & \vdots \\ C_{N,1} & C_{N,2} & \dots & C_{N,N} \end{pmatrix} \cdot \begin{pmatrix} n_1 \\ n_2 \\ \vdots \\ n_N \end{pmatrix},$$ (20)

and defining the vector and matrix quantities as

$$\boldsymbol{F} = \begin{pmatrix} n_1 \\ n_2 \\ \vdots \\ n_N \end{pmatrix} \quad and \quad \boldsymbol{C} = \begin{pmatrix} C_{1,1} & C_{1,2} & \dots & C_{1,N} \\ C_{2,1} & C_{2,2} & \dots & C_{2,N} \\ \vdots & \vdots & \ddots & \vdots \\ C_{N,1} & C_{N,2} & \dots & C_{N,N} \end{pmatrix}.$$ (21)

Equation (20) is written in the generalized vector representation

$$\frac{d\boldsymbol{F}}{ds} = \boldsymbol{C} \cdot \boldsymbol{F}.$$ (22)

In order to decouple the system of differential equations, the problem is solved using a thin shell approximation along the beam propagation characteristic interval $ds \approx s - s_o$, where the interval ds is small enough that an average constant value of the local plasma conditions and the collisional radiative matrix $\boldsymbol{C}$ can be assumed within the interval. Diagonalizing the average collisional radiative matrix for the interval $s_o \to s$,[12] the quasi-constant diagonal eigenvalues matrix $\boldsymbol{\lambda}$ and the eigenvectors matrix $\boldsymbol{V}$ are calculated. Using the linear transformations

$$\boldsymbol{F} = \boldsymbol{V} \cdot \boldsymbol{F}'$$

$$\boldsymbol{F}' = \boldsymbol{V}^{-1} \cdot \boldsymbol{F}$$

$$\boldsymbol{\lambda} = \boldsymbol{V}^{-1} \cdot \boldsymbol{C} \cdot \boldsymbol{V}.$$ (23)

Equation (20) is locally uncoupled and expressed as

$$\frac{d\boldsymbol{F}'}{ds} = \boldsymbol{\lambda} \cdot \boldsymbol{F}'.$$ (24)

Notice that the eigenvalues of the collisional radiative matrix represent the inverse values of the lifetimes for the populations of each individual nl-term in the model. Solving for the γ_{th}-element from Equation (24)

$$\frac{dn'_\gamma}{ds} = \lambda_\gamma n'_\gamma,$$ (25)

the solution is written as

$$n'_\gamma(s) = n'_\gamma(s_o) e^{\int_{s_o}^s \lambda_\gamma ds'}.$$ (26)

Since the average eigenvalue λ_γ within the interval $s_o \to s$ is assumed to be constant, the integral is reduced to $\int_{s_o}^s \lambda_\gamma ds' \approx \lambda_\gamma[s - s_o]$. Applying the linear transformations from Equations (23) to $n'_\gamma(s)$ and $n'_\gamma(s_o)$, and by using the characteristic relation $ds = dr/v_n$, the solution for the population densities is given by

$$n_{nl}(r) = \sum_{\gamma=1}^N V_{nl,\gamma} \sum_{\iota=1}^N V_{\gamma,\iota}^{-1} n_\iota(r_o) e^{\frac{1}{v_n} \lambda_\gamma [r-r_o]},$$ (27)

where the eigenvalue and eigenvector terms λ_γ, $V_{nl,\gamma}$, and $V_{\gamma,\iota}^{-1}$ correspond to those averaged for inside the small radial propagation interval $r_o \to r$, the calculated populations $n_{nl}(r)$ are used as the initial conditions $n_\iota(r_o)$ for the following interval calculation. It is initially assumed that all helium atoms in the gas-puff are on the ground state when first entering the plasma. For the smooth plasma profiles employed for the helium gas-puff simulation in this work (Figures 2 and 3), it was found that a small radial interval value of $dr = r - r_o \approx 5$ mm was enough to attain convergence. The length of the interval depends on the gradient of the plasma parameters along the propagation axis. The derived solution is similar to the time-dependent approach used by the HTD/I line-ratio model [Equation (21) of Ref. 12].

The final solution for the distribution function of the neutrals in the gas-puff [Equations (5) and (6)] within the small radial interval $dr = r - r_o$ is given by
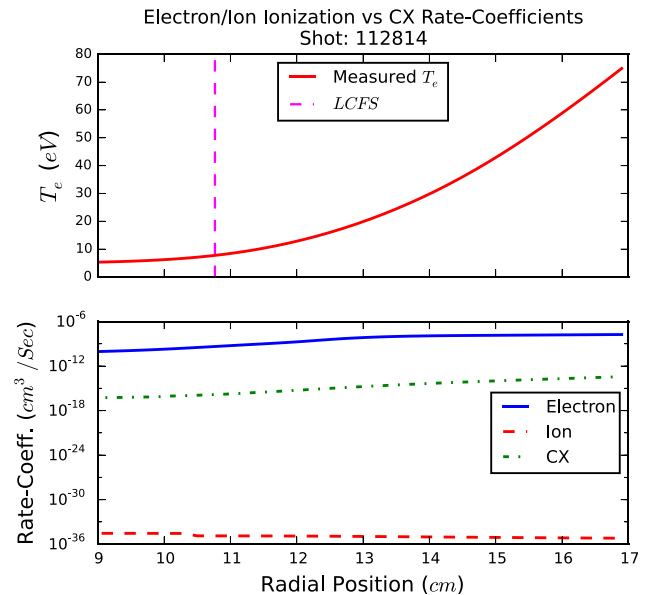

FIG. 2. Electron temperature radial profile obtained from fitting MPTS measurements from NSTX shot 112814. By assuming $T_i = T_e$,[19] electron/ion ionization and helium–deuteron charge-exchange (CX) rate-coefficients were calculated and compared. Electron-impact ionization is roughly six orders of magnitude higher than charge-exchange, and twenty five orders of magnitude higher than ion-impact ionization. It is definitely concluded that both charge-exchange and ion-ionization processes can be neglected in the SOL/edge regions. These results are consistent with the recently published DEGAS 2 Monte Carlo neutral transport simulations.[22,23]

$$f_{nl}(\boldsymbol{v}, \boldsymbol{r}, t) = f_o(\boldsymbol{v}) \sum_{\gamma=1}^{N} V_{nl,\gamma} \sum_{\iota=1}^{N} V_{\gamma,\iota}^{-1} n_\iota(r_o) e^{\frac{1}{v_n}\lambda_\gamma[r-r_o]}. \quad (28)$$

This model is used for predicting line emission of the helium gas-puff, and from the simulated emission, the electron temperature and densities as a function of the time-dependent line-ratios $[R(t)]$ are calculated using the HTD/I line-ratio model[12]

$$R_{T_e}(t) = \frac{I^{(706.5\,\mathrm{nm})}}{I^{(728.1\,\mathrm{nm})}}$$

$$R_{n_e}(t) = \frac{I^{(667.8\,\mathrm{nm})}}{I^{(728.1\,\mathrm{nm})}}$$

$$R_{T_e,n_e}(t) = \frac{I^{(706.5\,\mathrm{nm})}}{I^{(667.8\,\mathrm{nm})}}. \quad (29)$$

To assess the main neutral depletion processes that affect the penetration of the gas-puff into the SOL/edge regions of the plasma, electron ionization and helium–proton charge-exchange rate coefficients are calculated. For the sake of comparison, helium–proton ionization rate-coefficients were also calculated using the Percival and Richards expression by means of the "rqinew" ADAS subroutine,[20,21] although they may also be calculated from cross-sections using the generalized rate-coefficient expression from Equation (12).

Figure 2 shows the comparison between electron/ion ionization and charge-exchange rate-coefficients calculated using the measured MPTS electron temperature radial profile for NSTX shot 112814. In this work, the electron and ion temperatures were assumed to be equal $(T_i \approx T_e)$.[19] It is observed that the main interaction responsible for depleting the neutral gas-puff along the SOL and edge regions of the plasma [separated by the Last Closed Flux Surface (LCFS)] is electron ionization. It is therefore concluded that charge-exchange and ionization interactions with protons can be neglected. This conclusion agrees with recent DEGAS 2 Monte Carlo neutral transport simulations for deuterium gas-puffs on NSTX, where it was found that emission simulations in the SOL are insensitive to charge-exchange, including resonant charge-exchange processes.[22,23] Resonant charge-exchange processes between neutral deuterium and plasma deuterons are expected to be higher than those between helium and deuterons; therefore, as Figure 2 shows, the charge-exchange can be neglected.

The contributions of high Rydberg states to the lower $N = 19$ atomic populations $1snl$ $(1s < nl < 4f)$ are included by adding the projection matrix to the collisional radiative matrix [Equations (16) and (17)].[12] The details of the semi-empirical atomic data included in the projection matrix are given in Ref. 12. Figure 3 shows the modeled populations for the $1s3s(^3S)$, $1s3s(^1S)$, and $1s3d(^1D)$ atomic terms that correspond to the 706.7, 728.3, and 667.9 nm lines of helium, as well as the electron density profile for NSTX shot 112842 employed in the calculation. The model shows significant effects of high Rydberg contributions on the atomic populations, and how these contributions can affect the line emission radiation.
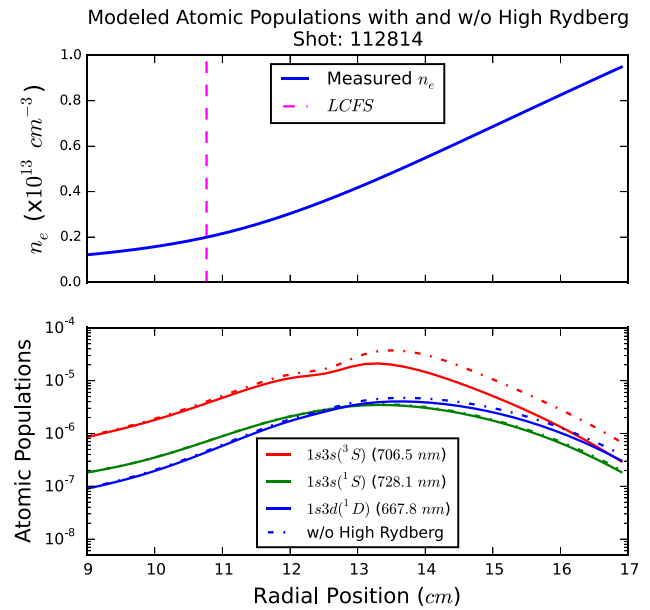

FIG. 3. Electron density radial profile from fitted MPTS measurements for NSTX shot 112814, and which is used [together with the electron temperature profile (Figure 2)] to calculate the atomic populations $1s3s(^3S)$, $1s3s(^1S)$, and $1s3d(^1D)$, which correspond to the 706.7, 728.3, and 667.9 lines. The calculation is done with and without (w/o dashed lines) high Rydberg contributions included in the collisional radiative matrix. Consistent with the previous results,[12] it is observed that high Rydberg contributions do affect significantly the atomic populations, particularly at the higher temperature and density regions of the SOL/edge.

The effects of high Rydberg contributions appear to increase with respect to electron temperature and density. These effects were also present when including high Rydberg contributions to the HTD/I line-ratio diagnostic to analyze emission data from TEXTOR.[12] It was experimentally observed that the helium line-ratio model without including high Rydberg contributions yielded closer electron temperature and density values with respect to those from MPTS measurements at TEXTOR (Figures 11 and 12 of Refs. 2 and 12). Based on these experimental results, emission calculations in this work included only the lower 19 configurations $1snl$ $(1s < nl < 4f)$.[12]

III. THERMAL HELIUM BEAM DIAGNOSTIC ON RFX-mod

To evaluate the application of the Thermal Helium Beam (THB) diagnostic from RFX-mod on NSTX-U, it is necessary to estimate the expected signal detection level for the three emission lines of helium (667.8, 706.5, and 728.1 nm). The most critical line is the 728.1 nm, since it is the weakest one of the three. In this section, a brief description of the THB diagnostic used in RFX-mod is given. A more complete discussion can be found in Ref. 3. The THB diagnostic uses the same equilibrium model from TEXTOR;[1] therefore, significantly different derived electron temperatures and densities between the THB and the HTD/I models are expected. These derived quantities differ not only due to the different atomic data sets employed but also due to the inclusion of the time relaxation effects in the atomic populations of the new model.[12]

To avoid complex transport calculations, the effects of electron recombination and recycle are experimentally subtracted. It is assumed that any neutral atom in the gas-puff that is ionized gets trapped in the magnetic field lines and transported away. This transported ion may eventually recycle or recombine and continue emitting at the same wavelengths as the neutrals from the gas injection. By subtracting the background and gas-puff signals, the recycle/recombination contributions are removed.[2,12]

Figure 4 shows an example of background subtraction used for data analysis on a single viewing-chord of the helium line-ratio spectral-monitoring (HELIOS) diagnostic that operated at TEXTOR.[2]

The THB diagnostic separates the three different helium emission wavelengths by means of a monochromator. The light collected from the plasma edge at 8 different radial locations is carried to the spectrograph through a bundle of optical fibers. The optics consists of a Czerny-Turner monochromator with a focal length of 300 mm and optical aperture of $f^{\#} = 4$, and a dispersive grating with 1200 lines/mm. At the light exit of the spectrograph, there are three slits of 1 mm width that are coupled to three arrays (one for each of the three wavelengths) of 8 viewing-chords (optical fibers). The light is then taken to three multi-anode photo-multiplier tubes (PMTs, Hamamatsu R5900U-20 L16) that are used as detectors for each of the wavelengths. The output signals of
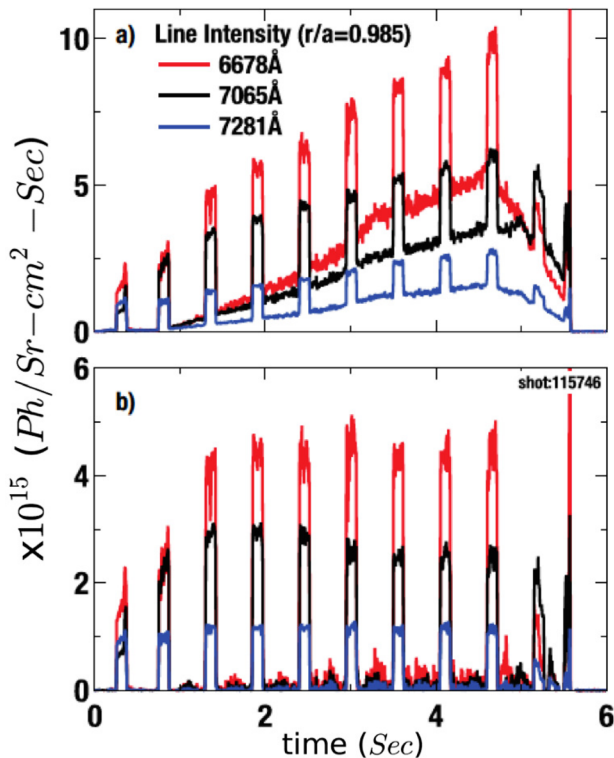
the PMTs are amplified and acquired with a sampling frequency of 2 MHz. The system is also equipped with a CCD camera that can acquire a complete spectrum of the collected light at a lower sampling rate, and the wavelength sensitivity calibration was obtained using an integrating sphere.

The characterization of the sensitivity of the diagnostic is needed to evaluate the feasibility of using the THB system for measuring helium line emission profiles on NSTX-U. Measuring the minimum measurable emission levels is critical, and these minimum values were compared to the expected intensities obtained from the simulated emissivities. The minimum signal levels were obtained from measurements of the three emission lines when the gas-puff signal can be discriminated from the background. The background is mainly due to the presence of signal from residual helium recycled on the graphite first wall in addition to low level electronic noise. During standard discharges on RFX-mod, the detected background emission produces an electronic signal at the output of the PMT amplifiers below 100 mV of the background signal. Therefore, the minimum signal level is set to 100 mV, which corresponds to the minimum measurable emission intensity.

Figure 5 shows the measured sensitivity curve for the 8 different viewing-chords of the THB system. This plot shows the minimum measurable emission for the three different wavelengths, which correspond to the minimum voltage signal (100 mV) at the output of the PMT amplifiers.

From sensitivity measurements using the actual optics and electronics, it is estimated that the lowest measured intensity value for detecting the 728.1 nm line is between $3.0 - 4.0 \times 10^{14} \, Ph/Sr - cm^2 - s$.

Figure 6 shows the radial profiles of the measured intensities of the three helium lines for a typical RFX-mod plasma discharge ($I_p = 1.5$ MA, and central electron density around $1.6 \times 10^{13} \, cm^{-3}$). Only six radial points are shown, and the other two viewing-chords were looking at a different toroidal and poloidal position. Figure 6 also shows electron

FIG. 4. Time history of helium gas-puff emission used in the line-ratio electron temperature and density diagnostic on the edge ($r/a = 0.985$) of the TEXTOR tokamak, where the pulses of intensity at $\sim$200 ms intervals for 100 ms are from the gas injector. (a) Total radiant intensity of each line including the background recycling/recombination light which builds up as the discharge evolves and helium gas is added. (b) Same data with the recycling/recombination light subtracted using a 100 ms rolling average smooth. Note: Line-ratio analysis is done individually for each of the helium gas-puff injection pulses.[2]
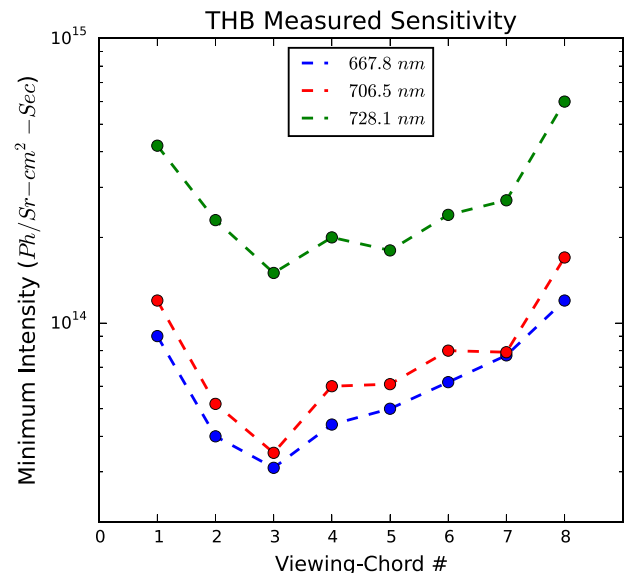

FIG. 5. Measured sensitivity limits of the THB system on RFX-mod for each of the eight viewing-chords. Measurements were performed for the three different helium wavelengths detected by the diagnostic.
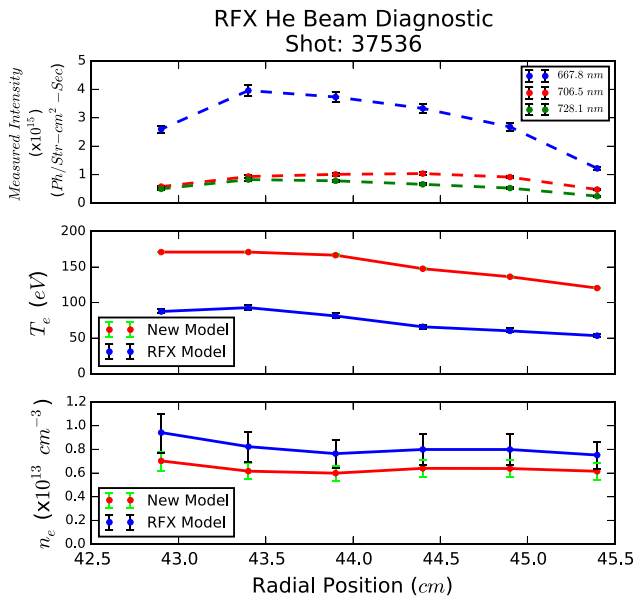
FIG. 6. Comparison between electron temperature and density radial profiles derived from measured intensity line-ratios using the RFX equilibrium model (TEXTOR model),[1] and the new HTD/I model[12] for RFX-mod shot 37536. The differences between the two are consistent with the previous results obtained at TEXTOR,[2,12] where it was found that including both the new atomic data set and the time-dependent evolution of the atomic populations yielded significant differences between the models.

temperature and density profiles derived using the RFX model (TEXTOR model),[1] and compared to those derived by the new HTD/I model.[12]

The results in Figure 6 show significant differences between the derived electron temperatures using the new HTD/I model,[12] and those from the TEXTOR model.[1] These differences are consistent with those previously obtained at TEXTOR, where it was observed that the electron temperatures derived from the HTD/I model showed better
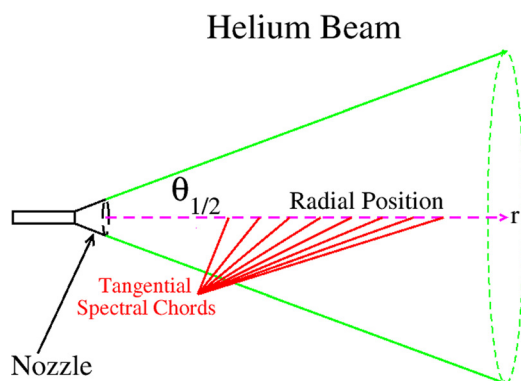

FIG. 7. Conical expansion profile employed to model the radial propagation of the thermal helium gas-puff with a half-angle expansion $\theta_{1/2}$. The radial position is measured from the output of the nozzle, while the spectral viewing-chords look at the beam radially and are oriented tangential to the toroidal vacuum vessel. The electron temperature and density profiles presented in Figures 2, 3, and 8 represent fitted MPTS measurements along the center of the radial axis. The tangentially located spectral viewing-chords are integrated through the 3-D conical expansion, which contain different electron temperatures and density values along the line-of-sight due to the angle of incidence and the crossing through different flux surfaces. The integrated emission is used to derive the original temperature and density profiles along the center of the beam, thus adding extra uncertainty to the results (Figure 8).

agreement to MPTS measurements, while the TEXTOR model highly underestimated the temperatures.[2,12] It was also observed that the new HTD/I model derived electron densities slightly closer to MPTS measurements.[12] The error analysis of the TEXTOR model includes two branches:[1] one is the systematic uncertainty from the atomic cross-sections and the integration procedures and assumptions to obtain rate-coefficients as discussed in Ref. 1. The second source of uncertainty is obtained from the measured line emissions. In this work, the measured uncertainty of the THB system on RFX-mod was estimated to be $\sim$5% relative to the line emission strength. This results in an uncertainty for the line-ratios, which yield an upper and lower margin for each. The uncertainties for the ratios were calculated with Gauss error propagation. Because the modeled line-ratios show non-linear dependencies on density and temperatures, the error propagation through the model yielded the results shown in Figure 6. Intensity measurements and uncertainties in the atomic data are also included in the error analysis of the HTD/I model, and they are explained in detail in Ref. 12.

IV. SIMULATED EMISSION ON NSTX/NSTX-U

For the analysis presented in this work, a single nozzle with a simple gas-puff conical expansion profile and a fixed half-angle expansion of $\theta_{1/2} \backsim 25^\circ$, which was estimated from camera observations of the NSTX Gas-Puff Imaging system (GPI), is considered (Figure 7).[24] The neutrals are propagated along the radial axis with a flow velocity v_n [Equation (7)] while they expand conically.
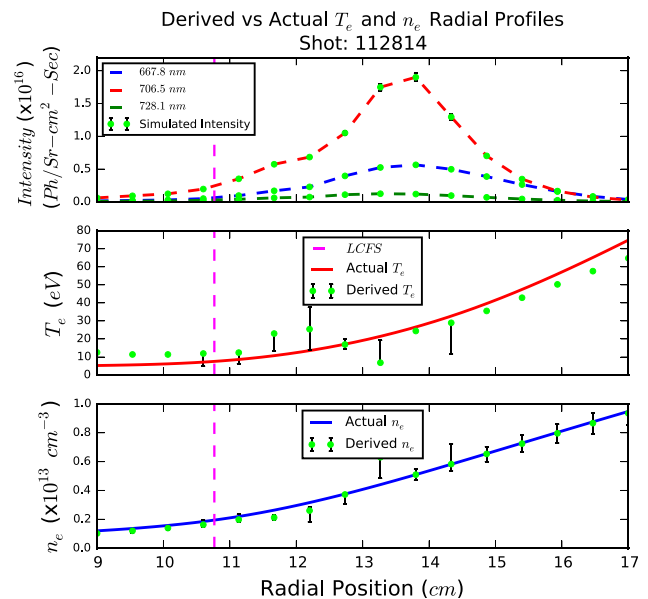
FIG. 8. Simulated line-of-sight integrated emission for the 667.8, 706.5, and 728.1 nm helium lines for NSTX shot 112824 using 16 spectral viewing-chords (Figure 7). The calculation was done assuming a gas source rate of 6.0×10^{20} Atoms/s,[24] and an uncertainty of $\pm3\%$ in the simulated intensities for error sensitivity analysis. The dashed lines help to reproduce a line emission profile by connecting the 16 simulated detection points. Line-ratios were calculated from the simulated emission to derive radial electron temperature and density profiles using the HTD/I model.[12] These profiles were compared to actual measurements along the center of the beam.

A total of 16 viewing-chords were considered. The numerical integration along the line-of-sight is performed between the two intersecting points of the spectral viewing-chord with the 3-D conical gas-puff expansion using Gauss–Legendre quadrature.[25] Convergence on the numerical integration was obtained with a minimum of 11 points. A total of 31 integration points were employed in the calculation. The 3-D mapping of the radial electron temperature and density profiles is taken into consideration when calculating local emissivities for each of the Gauss–Legendre points along the line-of-sight of each viewing-chord.

The measured electron temperature and density profiles (Figures 2 and 3) for the same NSTX shot (112814) as the GPI simulation were used to produce emission for the 667.8, 706.5, and 728.1 nm lines, as well as a gas-flow of 6.0 $\times 10^{20}$ Atoms/s.[24] For error analysis, an uncertainty of $\pm 3\%$ was artificially added to the simulated intensities. A detailed explanation of the error propagation employed on the new HTD/I model that includes both the uncertainties on the measured intensities and those estimated from the atomic data can be found in Ref. 12 Another source of uncertainty is intrinsically introduced by the 3-D integration along the line-of-sight through the conical expansion of the gas-puff, where different electron temperatures and densities are found due to the curvature of the flux lines. To reduce this source of uncertainty, the THB system would require a perpendicular viewing geometry with respect to the propagation axis of the thermal beam. The simulated lines were analyzed using the new HTD/I line-ratio model[12] to derive electron temperature and density profiles along the center of the radial axis. These results were compared to actual MPTS fitted measurements.

Figure 8 shows the simulated line-of-sight integrated emission calculated using the 1-D kinetic model. The figure also shows comparisons between the initial and derived electron temperature and density radial profiles obtained using the HTD/I model for NSTX shot 112814.

Another reason for scattering in the derived electron temperatures and densities is the resetting of initial atomic population values in the HTD/I model during the propagation time of the beam between data points, where the lifetimes of the atomic states are comparable to the transit time of the neutrals.[12] It was also found that the emission profile of the 728.1 nm line gets close to the signal detection limit $(3.0 - 4.0 \times 10^{14}\, Ph/Sr - cm^2 - s)$ of the RFX-mod system for some of the radial positions (Figure 8). Still for most of the profiles, the signal level remains above the detection limit, thus estimating a good signal level for application of the RFX-mod hardware to fast electron temperature and density measurements in the SOL/edge regions of NSTX-U. Measured electron temperatures and densities in the range of $T_e \backsim 20 \rightarrow 100\, eV$ and $n_e \backsim 2.0 \times 10^{12} \rightarrow 1.0 \times 10^{13}\, cm^{-3}$ are expected along the edge. The sensitivity of the THB can still be improved to reduce the detection limit by optimization of the $f^{\#} = 4$ spectrograph optical aperture, as well as designing a better coupling between optics and plasma. Another way to increase the signal level can be obtained by decreasing the bandwidth of the electronics, since the characteristic frequency of the edge fluctuations in tokamaks is lower then the one of reversed field pinches. The bandwidth
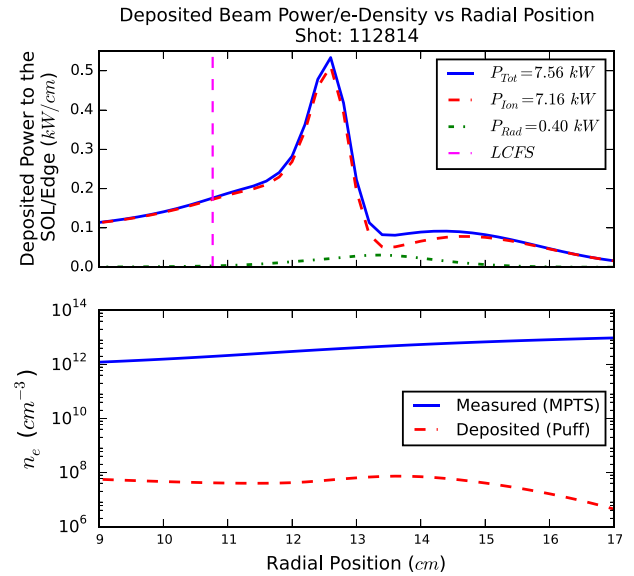

FIG. 9. Local deposited radial power and contributed electron density in the SOL/edge regions of NSTX by the helium neutral puff for shot 112824. The neutral puff functions as a power sink along the radial propagation direction, with most of the power dissipated by ionization rather than radiation.[1] The beam is ionized and the electrons get trapped and transported along the magnetic field lines to be redistributed along the SOL/edge plasma volume. The plasma volume was calculated using the NSTX EFIT equilibrium reconstruction.[27] The contributions of the puff to the electron density can be neglected, since local changes of both temperature and densities are $\leq 10\%$ for short pulses ($\tau_{puff} \sim 20$ ms).[26]

of the amplifier can be decreased from 2 MHz to 500 kHz in order to increase signal sensitivity. Finally, increasing the amount of helium in the gas-puff system would directly increase the line emission; however, opacity and local plasma perturbative effects must first be considered.

Improving the THB hardware will allow robust fast measurements ($\backsim 4\, \mu$s) of electron temperature and density profiles along the SOL/edge of NSTX-U for turbulence studies. Eventually, if this diagnostic is successful, a similar 2-D system may be used on the divertor region of NSTX-U.

Perturbative effects of deuterium and helium gas-puffs on the edge plasma of NSTX have been studied in detail for short pulses ($\tau_{puff} \sim 20$ ms).[26] It was observed that these puffs caused little or no change in the line-averaged plasma density or total stored energy, while the edge density and electron temperature changed by $\leq 10\%$, although in some discharges significant decrease in the electron temperature was observed $\sim$50–100 ms after the peak of the puff.[26] Figure 9 shows the calculated deposited radial power and contributed electron density from the neutral helium beam to the SOL/edge regions of NSTX for shot 112824.

Opacity effects on the measured spectral lines must also be considered when conducting gas-puff experiments for diagnostic and transport studies. Opacity effects were estimated using an escape factor code of the ADAS suite called ADAS214[20] and developed by Behringer.[28] A cylindrical plasma geometry with similar plasma conditions at the center of the conical expansion of the gas-puff was used. The calculation assumed a parabolic emission profile along the radius of the cylinder and Doppler emission profiles for the selected lines.[29] The escape factors were calculated for several lines of

TABLE I. Optical escape factors Λ calculated using the plasma conditions for NSTX shot 112824 for both helium and hydrogen lines at four different neutral densities n_o (cm^{-3}).

He λ (nm)	$n_o = 1 \times 10^{11}$	$n_o = 1 \times 10^{12}$	$n_o = 1 \times 10^{13}$	$n_o = 1 \times 10^{14}$
667.8	0.9357	0.5533	0.0635	0.0043
706.5	1.0000	0.9964	0.9784	0.8165
728.1	0.9945	0.9503	0.6354	0.0917
587.6	0.9986	0.9844	0.8598	0.3130
H λ (nm)	$n_o = 1 \times 10^{11}$	$n_o = 1 \times 10^{12}$	$n_o = 1 \times 10^{13}$	$n_o = 1 \times 10^{14}$
656.3	0.9025	0.4286	0.0383	0.0027
486.1	0.9857	0.8704	0.3353	0.0262
434.0	0.9960	0.9526	0.6482	0.0960

helium and deuterium that are important for line-ratio diagnostic [Equation (29)], and commonly used in turbulence studies.[22,26,30] Table I shows the estimated escape factors for four different neutral densities.

The opacity estimations show that for neutral densities $n_o \geq 10^{13}$ cm^{-3}, the neutral hydrogen cloud is opaque. These results consistent with those from Post.[31] Maximum neutral densities within the gas-puff deuterium cloud in the order of $\sim 5 \times 10^{12}$ cm^{-3} have been estimated.[26] Similar opacity results were found for helium lines, and from these estimations, it is concluded that local neutral densities for helium must be $n_o \leq 1 \times 10^{11}$ cm^{-3} in order to guaranty accurate electron temperature and density line-ratio measurements.

V. CONCLUSIONS

A 1-D kinetic collisional radiative solution was derived and used to simulate line-of-sight integrated emission along a helium gas-puff for three different spectral lines (667.8, 706.5, and 728.1 nm) that are commonly used for plasma diagnostic. It is concluded that excitation and ionization from electrons are the dominating collisional mechanisms that control the emission and depletion of the neutral cloud. It was estimated that both charge-exchange and ionization from main ions can be neglected since these processes are orders of magnitude lower than electron ionization. These results are consistent with recent gas-puff Monte Carlo simulations using DEGAS 2 for deuterium on NSTX, where it was found that resonant charge-exchange processes between neutral deuterium in the puff and plasma deuterons had a negligible effect on the emission and depletion of the gas.[22,23] Non-resonant charge-exchange between neutral helium and plasma deuterons is expected to be even lower.

It is also concluded that the effects of high Rydberg contributions to the lower atomic populations are significant, specially for the higher electron temperature and density regions of the SOL/edge. However, it was experimentally observed that when only the lower 19 configurations $1snl$ ($1s < nl < 4f$) were included in the collisional radiative model, closer to MPTS electron temperature and density measurements were derived than those that included high Rydberg.[12] Due to this experimental evidence, line emission simulations contained in this work did not include high Rydberg effects. Further experimental evidence is needed in order to do a complete assessment of high Rydberg effects on line emission.

The HTD/I helium line-ratio was used to derive electron temperature and density radial profiles from the experimental emission on RFX-mod. Results are consistent with those derived from TEXTOR,[2,12] which showed better agreement to MPTS measurements than the old model typically employed to analyze helium emission from the THB system on RFX-mod.[1]

The same atomic data set from the HTD/I helium line-ratio was employed on the 1-D kinetic model to simulate integrated helium gas-puff emission profiles for the 667.8, 706.5, and 728.1 nm lines on a bundle of 16 optical fibers for NSTX shot 112814. The simulated emission was analyzed using the HTD/I model[12] to closely reproduce the initial electron temperature and density profiles along the center of the propagation axis of the gas-puff. From these simulations, it is estimated that the expected signal level of the THB system on NSTX-U should be significantly larger than the detection limit, thus concluding that the application of this diagnostic to provide robust fast measurements ($\backsim 4 \mu$s) of electron temperature and density profiles along the SOL/edge of NSTX-U is a viable option.

Finally, it is concluded from opacity calculations that the amount of gas injected on NSTX-U will be limited by the local density of the neutrals at the spectral measurement points rather than perturbative effects on the local plasma parameters. Applications of a similar 2-D diagnostic system can eventually be expanded to the divertor region of NSTX-U in support of radiated power and detachment studies.

APPENDIX: DERIVATION OF THE GENERALIZED CHARGE-EXCHANGE RATE-COEFFICIENT

The generalized charge-exchange rate-coefficient [Equation (12)] is derived from the collision integral by using the shifted Maxwellian distribution functions for ions and neutrals given in Equations (3), (5), and (6), which may be written as

$$
\begin{aligned}
n_i \int d^3 \boldsymbol{v}\, q_{nl}^{CX}(\boldsymbol{v}) f_{nl} &= \int d^3 \boldsymbol{v} f_{nl}(\boldsymbol{v}, \boldsymbol{r}, t) \int d^3 \boldsymbol{v}' |\boldsymbol{v} - \boldsymbol{v}'| \\
&\quad \times \sigma_{nl}^{CX}(|\boldsymbol{v} - \boldsymbol{v}'|) f_i(\boldsymbol{v}') \\
&= \frac{n_i n_{nl}}{\pi^{3/2} v_{th_i}^3 v_{th_n}^3} \int d^3 \boldsymbol{v}\, e^{-(\boldsymbol{v} - \boldsymbol{v_n})^2 / v_{th_n}^2} \\
&\quad \times \int d^3 \boldsymbol{v}' |\boldsymbol{v} - \boldsymbol{v}'| \sigma_{nl}^{CX}(|\boldsymbol{v} - \boldsymbol{v}'|) e^{-(\boldsymbol{v}' - \boldsymbol{v_i})^2 / v_{th_i}^2}.
\end{aligned}
$$

(A1)

Since $|\boldsymbol{v} - \boldsymbol{v}'| = |\boldsymbol{v}' - \boldsymbol{v}|$, a new variable is defined as $\boldsymbol{u} = \boldsymbol{v}' - \boldsymbol{v}$. This yields $d^3\boldsymbol{u} = d^3\boldsymbol{v}'$; therefore,

$$n_i \int d^3\boldsymbol{v} q_{nl}^{CX}(\boldsymbol{v}) f_{nl} = \frac{2n_i n_{nl}}{\pi^2 v_{th_i}^3 v_{th_n}^3} \int d^3\boldsymbol{v} e^{-(\boldsymbol{v}-\boldsymbol{v}_n)^2/v_{th_n}^2} \times \int_0^\infty du u^3 \sigma_{nl}^{CX}(u) \int_0^\pi d\theta' \sin\theta' e^{-\left[u^2 + |\boldsymbol{v}-\boldsymbol{v}_i|^2 - 2u|\boldsymbol{v}-\boldsymbol{v}_i|\cos\theta'\right]/v_{th_i}^2}$$

$$= \frac{n_i n_{nl}}{\pi^2 v_{th_i} v_{th_n}^3} \int d^3\boldsymbol{v} \frac{1}{|\boldsymbol{v}-\boldsymbol{v}_i|} e^{-(\boldsymbol{v}-\boldsymbol{v}_i)^2/v_{th_i}^2} e^{-(\boldsymbol{v}-\boldsymbol{v}_n)^2/v_{th_n}^2} \times \int_0^\infty du u^2 \sigma_{nl}^{CX}(u) e^{-u^2/v_{th_i}^2} \left[e^{2u|\boldsymbol{v}-\boldsymbol{v}_i|/v_{th_i}^2} - e^{-2u|\boldsymbol{v}-\boldsymbol{v}_i|/v_{th_i}^2}\right].$$

(A2)

Changing variables to $\boldsymbol{\vartheta} = \boldsymbol{v} - \boldsymbol{v}_i$ and $d^3\boldsymbol{\vartheta} = d^3\boldsymbol{v}$, Equation (A2) can be written in the form

$$n_i \int d^3\boldsymbol{v} q_{nl}^{CX}(\boldsymbol{v}) f_{nl} = \frac{2n_i n_{nl}}{\pi v_{th_i} v_{th_n}^3} \int_0^\infty du u^2 \sigma_{nl}^{CX}(u) e^{-u^2/v_{th_i}^2} \times \int_0^\infty d\vartheta \vartheta \left[e^{-[\vartheta^2 - 2u\vartheta]/v_{th_i}^2} - e^{-[\vartheta^2 + 2u\vartheta]/v_{th_i}^2}\right]$$

$$\times \int_0^\pi d\theta \sin\theta e^{-\left[\vartheta^2 + |\boldsymbol{v}_i - \boldsymbol{v}_n|^2 + 2\vartheta|\boldsymbol{v}_i - \boldsymbol{v}_n|\cos\theta\right]/v_{th_n}^2}$$

$$= \frac{n_i n_{nl}}{\pi v_{th_i} v_{th_n}} \frac{1}{|\boldsymbol{v}_i - \boldsymbol{v}_n|} \int_0^\infty du u^2 \sigma_{nl}^{CX}(u) e^{-u^2/v_{th_i}^2} \times \int_0^\infty d\vartheta \left[e^{-[\vartheta^2 - 2u\vartheta]/v_{th_i}^2} - e^{-[\vartheta^2 + 2u\vartheta]/v_{th_i}^2}\right]$$

$$\times \left[e^{-[\vartheta^2 + |\boldsymbol{v}_i - \boldsymbol{v}_n|^2 - 2\vartheta|\boldsymbol{v}_i - \boldsymbol{v}_n|]/v_{th_n}^2} - e^{-[\vartheta^2 + |\boldsymbol{v}_i - \boldsymbol{v}_n|^2 + 2\vartheta|\boldsymbol{v}_i - \boldsymbol{v}_n|]/v_{th_n}^2}\right],$$

(A3)

and also expressed as

$$n_i \int d^3\boldsymbol{v} q_{nl}^{CX}(\boldsymbol{v}) f_{nl} = \frac{n_i n_{nl}}{\pi v_{th_i} v_{th_n}} \frac{1}{|\boldsymbol{v}_i - \boldsymbol{v}_n|} e^{-(\boldsymbol{v}_i - \boldsymbol{v}_n)^2/v_{th_n}^2} \int_0^\infty du u^2 \sigma_{nl}^{CX}(u) e^{-u^2/v_{th_i}^2}$$

$$\times \int_0^\infty d\vartheta \left\{ e^{-\left[\left(\frac{v_{th_i}^2 + v_{th_n}^2}{v_{th_i}^2 v_{th_n}^2}\right)\vartheta^2 - 2\left(\frac{v_{th_n}^2 u + v_{th_i}^2 |\boldsymbol{v}_i - \boldsymbol{v}_n|}{v_{th_i}^2 v_{th_n}^2}\right)\vartheta\right]} - e^{-\left[\left(\frac{v_{th_i}^2 + v_{th_n}^2}{v_{th_i}^2 v_{th_n}^2}\right)\vartheta^2 - 2\left(\frac{v_{th_n}^2 u - v_{th_i}^2 |\boldsymbol{v}_i - \boldsymbol{v}_n|}{v_{th_i}^2 v_{th_n}^2}\right)\vartheta\right]}\right.$$

$$\left. - e^{-\left[\left(\frac{v_{th_i}^2 + v_{th_n}^2}{v_{th_i}^2 v_{th_n}^2}\right)\vartheta^2 + 2\left(\frac{v_{th_n}^2 u - v_{th_i}^2 |\boldsymbol{v}_i - \boldsymbol{v}_n|}{v_{th_i}^2 v_{th_n}^2}\right)\vartheta\right]} + e^{-\left[\left(\frac{v_{th_i}^2 + v_{th_n}^2}{v_{th_i}^2 v_{th_n}^2}\right)\vartheta^2 + 2\left(\frac{v_{th_n}^2 u + v_{th_i}^2 |\boldsymbol{v}_i - \boldsymbol{v}_n|}{v_{th_i}^2 v_{th_n}^2}\right)\vartheta\right]}\right\}.$$

(A4)

Each of the integrals with respect to ϑ can be solved by completing the square of the exponent, and by changing variables to x can be written in the form

$$\int_0^\infty d\vartheta e^{-[a\vartheta^2 + 2b\vartheta]} = e^{b^2/a} \int_0^\infty d\vartheta e^{-\left[\sqrt{a}\vartheta + b/\sqrt{a}\right]^2} = \frac{1}{\sqrt{a}} e^{b^2/a} \int_{b/\sqrt{a}}^\infty dx e^{-x^2},$$

(A5)

and which solution is related to the complementary error function defined as

$$Erfc(t) = \frac{2}{\sqrt{\pi}} \int_t^\infty dx e^{-x^2}.$$

(A6)

Therefore, Equation (A4) can be written in the form

$$n_i \int d^3\boldsymbol{v} q_{nl}^{CX}(\boldsymbol{v}) f_{nl} = \frac{n_i n_{nl}}{2\sqrt{\pi}} \frac{1}{\sqrt{v_{th_i}^2 + v_{th_n}^2}} \frac{1}{|\boldsymbol{v}_i - \boldsymbol{v}_n|} \int_0^\infty du u^2 \sigma_{nl}^{CX}(u)$$

$$\times \left\{ e^{-\left[\frac{(u - |\boldsymbol{v}_i - \boldsymbol{v}_n|)^2}{(v_{th_i}^2 + v_{th_n}^2)}\right]} \left(Erfc\left[-\frac{\left(u + \frac{v_{th_i}^2}{v_{th_n}^2}|\boldsymbol{v}_i - \boldsymbol{v}_n|\right)}{\frac{v_{th_i}}{v_{th_n}}\sqrt{v_{th_i}^2 + v_{th_n}^2}}\right] + Erfc\left[\frac{\left(u + \frac{v_{th_i}^2}{v_{th_n}^2}|\boldsymbol{v}_i - \boldsymbol{v}_n|\right)}{\frac{v_{th_i}}{v_{th_n}}\sqrt{v_{th_i}^2 + v_{th_n}^2}}\right]\right) \right.$$

$$\left. - e^{-\left[\frac{(u + |\boldsymbol{v}_i - \boldsymbol{v}_n|)^2}{(v_{th_i}^2 + v_{th_n}^2)}\right]} \left(Erfc\left[-\frac{\left(u - \frac{v_{th_i}^2}{v_{th_n}^2}|\boldsymbol{v}_i - \boldsymbol{v}_n|\right)}{\frac{v_{th_i}}{v_{th_n}}\sqrt{v_{th_i}^2 + v_{th_n}^2}}\right] + Erfc\left[\frac{\left(u - \frac{v_{th_i}^2}{v_{th_n}^2}|\boldsymbol{v}_i - \boldsymbol{v}_n|\right)}{\frac{v_{th_i}}{v_{th_n}}\sqrt{v_{th_i}^2 + v_{th_n}^2}}\right]\right)\right\}.$$

(A7)

Using the property of the complementary error function $Erfc(-t) + Erfc(t) = 2$, Equation (A7) is reduced to

$$n_i \int d^3 v q_{nl}^{CX}(v) f_{nl} = \frac{n_i n_{nl}}{\sqrt{\pi}} \frac{1}{\sqrt{v_{th_i}^2 + v_{th_n}^2}} \frac{1}{|v_i - v_n|} \int_0^\infty du u^2 \sigma_{nl}^{CX}(u) \times \left\{ e^{-\left[\frac{(u-|v_i-v_n|)^2}{(v_{th_i}^2 + v_{th_n}^2)}\right]} - e^{-\left[\frac{(u+|v_i-v_n|)^2}{(v_{th_i}^2 + v_{th_n}^2)}\right]} \right\}. \tag{A8}$$

This equation suggests that the maximum value of the generalized charge-exchange integral will occur for differential velocities $u \approx |v_i - v_n|$ ($u = v' - v$). The equation can be simplified further by expressing the integral kernel in terms of a hyperbolic sine function

$$n_i \int d^3 v q_{nl}^{CX}(v) f_{nl} = \frac{n_i n_{nl}}{\sqrt{\pi}} \frac{1}{\sqrt{v_{th_i}^2 + v_{th_n}^2}} \frac{1}{|v_i - v_n|} e^{-(v_i-v_n)^2/(v_{th_i}^2 + v_{th_n}^2)} \int_0^\infty du u^2 \sigma_{nl}^{CX}(u) e^{-u^2/(v_{th_i}^2 + v_{th_n}^2)}$$

$$\times \left\{ e^{\left[\frac{2|v_i-v_n|}{(v_{th_i}^2 + v_{th_n}^2)}u\right]} - e^{-\left[\frac{2|v_i-v_n|}{(v_{th_i}^2 + v_{th_n}^2)}u\right]} \right\}$$

$$= \frac{2 n_i n_{nl}}{\sqrt{\pi}} \frac{1}{\sqrt{v_{th_i}^2 + v_{th_n}^2}} \frac{1}{|v_i - v_n|} e^{-(v_i-v_n)^2/(v_{th_i}^2 + v_{th_n}^2)} \int_0^\infty du u^2 \sigma_{nl}^{CX}(u) e^{-u^2/(v_{th_i}^2 + v_{th_n}^2)} \times \sinh\left[\frac{2|v_i-v_n|}{(v_{th_i}^2 + v_{th_n}^2)}u\right]. \tag{A9}$$

Changing variables to the non-dimensional variable $\nu = u / \sqrt{v_{th_i}^2 + v_{th_n}^2}$, and defining

$$n_i \int d^3 v q_{nl}^{CX}(v) f_{nl} = n_i n_{nl} Q_{nl}^{CX}, \tag{A10}$$

the generalized charge-exchange rate-coefficient is written in its final form as

$$Q_{nl}^{CX} = \frac{2}{\sqrt{\pi}} \frac{\left(v_{th_i}^2 + v_{th_n}^2\right)}{|v_i - v_n|} e^{-(v_i-v_n)^2/(v_{th_i}^2 + v_{th_n}^2)}$$

$$\times \int_0^\infty d\nu \nu^2 \sinh\left[\frac{2|v_i - v_n|}{\sqrt{v_{th_i}^2 + v_{th_n}^2}} \nu\right] \sigma_{nl}^{CX}(\nu) e^{-\nu^2}. \tag{A11}$$

The non-dimensional variable ν can be related to the center-of-mass energy of the charge-exchange cross-section with

$$E(\text{eV/amu}) = \frac{m_{amu}}{2e}\left(v_{th_i}^2 + v_{th_n}^2\right)\nu^2. \tag{A12}$$

The generalized rate-coefficient from Equation (A11) can be integrated numerically using Gauss–Legendre quadrature.[25] This expression is similar to the one derived in Ref. 23, where the rates were written in terms of the $I_{l,n}$ integrals that are stored in DEGAS 2.

For the special case that $v_i \approx v_n$ or $|v_i - v_n| \to 0$, it can be shown that Equation (A11) is reduced to

$$Q_{nl}^{CX} = \frac{4}{\sqrt{\pi}} \sqrt{v_{th_i}^2 + v_{th_n}^2} \int_0^\infty d\nu \nu^3 \sigma_{nl}^{CX}(\nu) e^{-\nu^2}. \tag{A13}$$

[1] O. Schmitz, I. L. Beigman, L. A. Vainshtein, B. Schweer, M. Kantor, A. Pospieszczyk, Y. Xu, M. Krychowlak, M. Lehnen, U. Samm, B. Unterberg, and the TEXTOR Team, Plasma Phys. Controlled Fusion **50**, 115004 (2008).

[2] E. A. Unterberg, O. Schmitz, D. H. Fehling, H. Stoschus, C. C. Klepper, J. M. Muñoz-Burgos, G. Van Wassenhove, and D. L. Hillis, Rev. Sci. Instrum. **83**, 10D722 (2012).

[3] M. Agostini, P. Scarin, R. Cavazzana, A. Fassina, A. Alfier, and N. Vianello, Rev. Sci. Instrum. **81**, 10D715 (2010).

[4] A. Pospieszczyk, G. Chevalier, Y. Hirooka, R. W. Conn, R. Doerner, and L. Schmitz, Nucl. Instrum. Methods Phys. Res. **B72**, 207223 (1992).

[5] Y. Andrew and M. G. O'Mullane, Plasma Phys. Controlled Fusion **42**, 301–307 (2000).

[6] H. Kubo, M. Goto, H. Takenaga, A. Kumagai, T. Sugie, S. Sakurai, N. Asakura, S. Higashijima, and A. Sakasai, J. Plasma Fusion Res. **75**, 945 (1999).

[7] R. J. Maqueda, G. A. Wurden, S. Zweben, L. Roquemore, H. Kugel, D. Johnson, S. Kaye, S. Sabbagh, and R. Maingi, Rev. Sci. Instrum. **72**, No. 1 (2001).

[8] S. Lisgo, P. Börner, G. F. Counsell, J. Dowling, A. Kirk, R. Scannell, M. G. O'Mullane, D. Reiter, and The MAST Team, J. Nucl. Mater. **390–391**, 1078–1080 (2009).

[9] M. Agostini, P. Scarin, G. Spizzo, N. Vianello, and L. Carraro, Plasma Phys. Controlled Fusion **56**, 095016 (2014).

[10] M. Agostini, P. Scarin, R. Cavazzana, F. Sattin, G. Serianni, M. Spolaore, and N. Vianello, Plasma Phys. Controlled Fusion **51**, 105003 (2009).

[11] J. M. Muñoz Burgos, S. D. Loch, C. P. Ballance, and R. F. Boivin, Astron. Astrophys. **500**, 1253–1261 (2009).

[12] J. M. Muñoz Burgos, O. Schmitz, S. D. Loch, and C. P. Ballance, Phys. Plasmas **19**, 012501 (2012).

[13] P. G. Burke and K. A. Berrington, *Atomic and Molecular Processes: An R-Matrix Approach* (Institute of Publishing (IOP), Bristol, 1993).

[14] K. Bartschat, Comput. Phys. Commun. **114**, 168 (1998).

[15] I. Bray and A. T. Stelbovics, Phys. Rev. A **46**, 6995 (1992).

[16] D. V. Fursa and I. Bray, Phys. Rev. A **52**, 1279 (1995).

[17] J. Loreau, S. Ryabchenko, and N. Vaeck, J. Phys. B: At. Mol. Opt. Phys. **47**, 135204 (2014).

[18] V. A. Soukhanovskii, R. Kaita, R. Majeski, and A. L. Roquemore, Rev. Sci. Instrum. **75**, 4320 (2004).

[19] P. C. Stangeby, *The Plasma Boundary of Magnetic Fusion Devices* (Taylor & Fancis Group, New York, NY, 2000), p. 15.

[20]H. P. Summers, The ADAS User Manual, version 2.6, http://www.adas.ac.uk, 2004.

[21]I. C. Percival and D. Richards, J. Phys. B: At. Mol. Opt. Phys. **3**, 1035 (1970).

[22]D. P. Stotler, F. Scotti, R. E. Bell, A. Diallo, B. P. LeBlanc, M. Podesta, A. L. Roquemore, and P. W. Ross, Phys. Plasmas **22**, 082506 (2015).

[23]D. P. Stotler, C. S. Chang, G. Park, and S. H. Ku, Comput. Sci. Disc. **6**, 015006 (2013).

[24]D. P. Stotler, J. Boedo, B. LeBlanc, R. J. Maqueda, and S. J. Zweben, J. Nucl. Mater. **363**, 686–692 (2007).

[25]W. H. Press, S. A. Teukolsky, W. T. Vetterling, and B. P. Flannery, *Numerical Recipes the Art of Scientific Computing*, 3rd ed. (Cambridge University Press, New York, 2007).

[26]S. J. Zweben, D. P. Stotler, R. E. Bell, W. M. Davis, S. M. Kaye, B. P. LeBlanc, R. J. Maqueda, E. T. Meier, T. Munsat, Y. Ren, S. A. Sabbagh, Y. Sechrest, D. R. Smith, and V. Soukhanovskii, Plasma Phys. Controlled Fusion **56**, 095010 (2014).

[27]S. A. Sabbagh, J. W. Ahn, J. Allain, R. Andre, A. Balbaky, R. Bastasz, D. Battaglia, M. Bell, R. Bell, P. Beiersdorfer, E. Belova, J. Berkery, R. Betti, J. Bialek, T. Bigelow, M. Bitter, J. Boedo, P. Bonoli, A. Boozer, A. Bortolon, D. Boyle, D. Brennan, J. Breslau, R. Buttery, J. Canik, G. Caravelli, C. Chang, N. Crocker, D. Darrow, B. Davis, L. Delgado-Aparicio, A. Diallo, S. Ding, D. D'Ippolito, C. Domier, W. Dorland, S. Ethier, T. Evans, J. Ferron, M. Finkenthal, J. Foley, R. Fonck, R. Frazin, E. Fredrickson, G. Fu, D. Gates, S. Gerhardt, A. Glasser, N. Gorelenkov, T. Gray, Y. Guo, W. Guttenfelder, T. Hahm, R. Harvey, A. Hassanein, W. Heidbrink, K. Hill, Y. Hirooka, E. B. Hooper, J. Hosea, D. Humphreys, K. Indireshkumar, F. Jaeger, T. Jarboe, S. Jardin, M. Jaworski, R. Kaita, J. Kallman, O. Katsuro-Hopkins, S. Kaye, C. Kesse, J. Kim, E. Kolemen, G. Kramer, S. Krasheninnikov, S. Kubota, H. Kuge, R. J. La Haye, L. Lao, B. LeBlanc, W. Lee, K. Lee, J. Leuer, F. Levinton, Y. Liang, D. Liu, J. Lore, N. Luhmann Jr, R. Maingi, R. Majeski, J. Manickam, D. Mansfield, R. Maqueda, E. Mazzucato, A. McLean, D. McCune, B. McGeehan, G. McKee, S. Medley, E. Meier, J. Menard, M. Menon, H. Meyer, D. Mikkelsen, G. Miloshevsky, D. Mueller, T. Munsat, J. Myra, B. Nelson, N. Nishino, R. Nygren, M. Ono, T. Osborne, H. Park, J. Park, Y. S. Park, S. Paul, W. Peebles, B. Penaflor, R. J. Perkins, C. Phillips, A. Pigarov, M. Podesta, J. Preinhaelter, R. Raman, Y. Ren, G. Rewoldt, T. Rognlien, P. Ross, C. Rowley, E. Ruskov, D. Russell, D. Ruzic, P. Ryan, M. Schaffer, E. Schuster, F. Scotti, K. Shaing, V. Shevchenko, K. Shinohara, V. Sizyuk, C. H. Skinner, A. Smirnov, D. Smith, P. Snyder, W. Solomon, A. Sontag, V. Soukhanovskii, T. Stoltzfus-Dueck, D. Stotler, B. Stratton, D. Stutman, H. Takahashi, Y. Takase, N. Tamura, X. Tang, G. Taylor, C. Taylor, K. Tritz, D. Tsarouhas, M. Umansky, J. Urban, E. Untergberg, M. Walker, W. Wampler, W. Wang, J. Whaley, R. White, J. Wilgen, R. Wilson, K. L. Wong, J. Wright, Z. Xia, D. Youchison, G. Yu, H. Yuh, L. Zakharov, D. Zemlyanov, G. Zimmer, and S. J. Zweben, Nucl. Fusion **41**, 1601 (2001).

[28]K. Behringer and U. Fantz, New J. Phys. **2**, 23 (2000).

[29]N. K. Podder, J. A. Johnson III, C. T. Raynor, S. D. Loch, C. P. Ballance, and M. S. Pindzola, Phys. Plasmas **11**, 5436–5443 (2004).

[30]R. J. Maqueda, G. A. Wurden, D. P. Stotler, S. J. Zweben, B. LaBombard, J. L. Terry, J. L. Lowrance, V. J. Mastrocola, G. F. Renda, D. A. D'Ippolito, J. R. Myra, and N. Nishino, Rev. Sci. Instrum. **74**, 2020 (2003).

[31]D. E. Post, J. Nucl. Mater. **220–222**, 143–157 (1995).